

Andrews University

Digital Commons @ Andrews University

Faculty Publications

4-1-2007

Measurement of Open Beauty Production at HERA in the D^{*}M Final State

S. Chekanov

Argonne National Laboratory

M. Derrick

Argonne National Laboratory

S. Magill

Argonne National Laboratory

S. Miglioranzi

Argonne National Laboratory

B. Musgrave

Argonne National Laboratory

See next page for additional authors

Follow this and additional works at: <https://digitalcommons.andrews.edu/pubs>



Part of the [Physics Commons](#)

Recommended Citation

Chekanov, S.; Derrick, M.; Magill, S.; Miglioranzi, S.; Musgrave, B.; Nicholass, D.; Repond, J.; Yoshida, R.; Mattingly, Margarita C. K.; Pavel, N.; Yagües Molina, A. G.; Antonelli, S.; Antonioli, P.; Bari, G.; Basile, M.; Bellagamba, L.; Bindi, M.; Boscherini, D.; Bruni, A.; Bruni, G.; Cifarelli, L.; Cindolo, F.; Contin, A.; Corradi, M.; De Pasquale, S.; Iacobucci, G.; Margotti, A.; Nania, R.; Polini, A.; Rinaldi, L.; and Sartorelli, G., "Measurement of Open Beauty Production at HERA in the D^{*}M Final State" (2007). *Faculty Publications*. 1813. <https://digitalcommons.andrews.edu/pubs/1813>

This Article is brought to you for free and open access by Digital Commons @ Andrews University. It has been accepted for inclusion in Faculty Publications by an authorized administrator of Digital Commons @ Andrews University. For more information, please contact repository@andrews.edu.

Authors

S. Chekanov, M. Derrick, S. Magill, S. Miglioranzi, B. Musgrave, D. Nicholass, J. Repond, R. Yoshida, Margarita C. K. Mattingly, N. Pavel, A. G. Yagües Molina, S. Antonelli, P. Antonioli, G. Bari, M. Basile, L. Bellagamba, M. Bindi, D. Boscherini, A. Bruni, G. Bruni, L. Cifarelli, F. Cindolo, A. Contin, M. Corradi, S. De Pasquale, G. Iacobucci, A. Margotti, R. Nania, A. Polini, L. Rinaldi, and G. Sartorelli

Measurement of open beauty production at HERA in the $D^* \mu$ final state

The ZEUS Collaboration

S. Chekanov^{1,a}, M. Derrick¹, S. Magill¹, S. Miglioranzi^{1,b}, B. Musgrave¹, D. Nicholass^{1,a}, J. Repond¹, R. Yoshida¹, M.C.K. Mattingly², N. Pavel^{3,†}, A.G. Yagües Molina³, S. Antonelli⁴, P. Antonioli⁴, G. Bari⁴, M. Basile⁴, L. Bellagamba⁴, M. Bindi⁴, D. Boscherini⁴, A. Bruni⁴, G. Bruni⁴, L. Cifarelli⁴, F. Cindolo⁴, A. Contin⁴, M. Corradi^{4,c}, S. De Pasquale⁴, G. Iacobucci⁴, A. Margotti⁴, R. Nania⁴, A. Polini⁴, L. Rinaldi⁴, G. Sartorelli⁴, A. Zichichi⁴, G. Aghuzumtsyan^{5,d}, D. Bartsch⁵, I. Brock⁵, S. Goers⁵, H. Hartmann⁵, E. Hilger⁵, H.-P. Jakob⁵, M. Jüngst⁵, O.M. Kind⁵, E. Paul^{5,e}, J. Rautenberg^{5,f}, R. Renner⁵, U. Samson^{5,g}, V. Schönberg⁵, M. Wang⁵, M. Wlasenko⁵, N.H. Brook⁶, G.P. Heath⁶, J.D. Morris⁶, T. Namsoo⁶, M. Capua⁷, S. Fazio⁷, A. Mastroberardino⁷, M. Schioppa⁷, G. Susinno⁷, E. Tassi⁷, J.Y. Kim^{8,h}, K.J. Ma^{8,i}, Z.A. Ibrahim⁹, B. Kamaluddin⁹, W.A.T. Wan Abdullah⁹, Y. Ning¹⁰, Z. Ren¹⁰, F. Sciulli¹⁰, J. Chwastowski¹¹, A. Eskreys¹¹, J. Figiel¹¹, A. Galas¹¹, M. Gil¹¹, K. Olkiewicz¹¹, P. Stopa¹¹, L. Zawiejski¹¹, L. Adamczyk¹², T. Bold¹², I. Grabowska-Bold¹², D. Kisielewska¹², J. Lukasik¹², M. Przybycien¹², L. Suszycki¹², A. Kotański^{13,j}, W. Słomiński¹³, V. Adler¹⁴, U. Behrens¹⁴, I. Bloch¹⁴, A. Bonato¹⁴, K. Borras¹⁴, N. Coppola¹⁴, J. Fourletova¹⁴, A. Geiser¹⁴, D. Gladkov¹⁴, P. Göttlicher^{14,k}, I. Gregor¹⁴, T. Haas¹⁴, W. Hain¹⁴, C. Horn¹⁴, B. Kahle¹⁴, U. Kötz¹⁴, H. Kowalski¹⁴, E. Lobodzinska¹⁴, B. Lühr¹⁴, R. Mankel¹⁴, I.-A. Melzer-Pellmann¹⁴, A. Montanari¹⁴, D. Notz¹⁴, A.E. Nuncio-Quiroz¹⁴, R. Santamarta¹⁴, U. Schneekloth¹⁴, A. Spiridonov^{14,l}, H. Stadie¹⁴, U. Stösslein¹⁴, D. Szuba^{14,m}, J. Szuba^{14,n}, T. Theedt¹⁴, G. Wolf¹⁴, K. Wrona¹⁴, C. Youngman¹⁴, W. Zeuner¹⁴, S. Schlenstedt¹⁵, G. Barbagli¹⁶, E. Gallo^{16,o}, P.G. Pelfer¹⁶, A. Bamberger¹⁷, D. Dobur¹⁷, F. Karstens¹⁷, N.N. Vlasov^{17,p}, P.J. Bussey¹⁸, A.T. Doyle¹⁸, W. Dunne¹⁸, J. Ferrando¹⁸, D.H. Saxon¹⁸, I.O. Skillicorn¹⁸, I. Gialas^{19,q}, T. Gosau²⁰, U. Holm²⁰, R. Klanner²⁰, E. Lohrmann²⁰, H. Salehi²⁰, P. Schleper²⁰, T. Schörner-Sadenius²⁰, J. Sztuk²⁰, K. Wichmann²⁰, K. Wick²⁰, C. Foudas²¹, C. Fry²¹, K.R. Long²¹, A.D. Tapper²¹, M. Kataoka^{22,r}, T. Matsumoto²², K. Nagano²², K. Tokushuku^{22,s}, S. Yamada²², Y. Yamazaki²², A.N. Barakbaev²³, E.G. Boos²³, A. Dossanov²³, N.S. Pokrovskiy²³, B.O. Zhautykov²³, D. Son²⁴, J. de Favereau²⁵, K. Piotrkowski²⁵, F. Barreiro²⁶, C. Glasman^{26,t}, M. Jimenez²⁶, L. Labarga²⁶, J. del Peso²⁶, E. Ron²⁶, J. Terrón²⁶, M. Zambrana²⁶, F. Corriveau²⁷, C. Liu²⁷, R. Walsh²⁷, C. Zhou²⁷, T. Tsurugai²⁸, A. Antonov²⁹, B.A. Dolgoshein²⁹, I. Rubinsky²⁹, V. Sosnovtsev²⁹, A. Stifutkin²⁹, S. Suchkov²⁹, R.K. Dementiev³⁰, P.F. Ermolov³⁰, L.K. Gladilin³⁰, I.I. Katkov³⁰, L.A. Khein³⁰, I.A. Korzhavina³⁰, V.A. Kuzmin³⁰, B.B. Levchenko^{30,u}, O.Y. Lukina³⁰, A.S. Proskuryakov³⁰, L.M. Shcheglova³⁰, D.S. Zotkin³⁰, S.A. Zotkin³⁰, I. Abt³¹, C. Büttner³¹, A. Caldwell³¹, D. Kollar³¹, W.B. Schmidke³¹, J. Sutiak³¹, G. Grigorescu³², A. Keramidas³², E. Koffeman³², P. Kooijman³², A. Pellegrino³², H. Tieceke³², M. Vázquez^{32,r}, L. Wiggers³², N. Brümmer³³, B. Bylsma³³, L.S. Durkin³³, A. Lee³³, T.Y. Ling³³, P.D. Allfrey³⁴, M.A. Bell³⁴, A.M. Cooper-Sarkar³⁴, A. Cottrell³⁴, R.C.E. Devenish³⁴, B. Foster³⁴, K. Korcsak-Gorzo³⁴, S. Patel³⁴, V. Roberfroid^{34,v}, A. Robertson³⁴, P.B. Straub³⁴, C. Uribe-Estrada³⁴, R. Walczak³⁴, P. Bellan³⁵, A. Bertolin³⁵, R. Brugnera³⁵, R. Carlin³⁵, R. Ciesielski³⁵, F. Dal Corso³⁵, S. Dusini³⁵, A. Garfagnini³⁵, S. Limentani³⁵, A. Longhin³⁵, L. Stanco³⁵, M. Turcato³⁵, B.Y. Oh³⁶, A. Raval³⁶, J. Ukleja^{36,w}, J.J. Whitmore³⁶, Y. Iga³⁷, G. D'Agostini³⁸, G. Marini³⁸, A. Nigro³⁸, J.E. Cole³⁹, J.C. Hart³⁹, H. Abramowicz^{40,x}, A. Gabareen⁴⁰, R. Ingbir⁴⁰, S. Kananov⁴⁰, A. Levy⁴⁰, M. Kuze⁴¹, R. Hori⁴², S. Kagawa^{42,y}, N. Okazaki⁴², S. Shimizu⁴², T. Tawara⁴², R. Hamatsu⁴³, H. Kaji^{43,z}, S. Kitamura^{43,aa}, O. Ota⁴³, Y.D. Ri⁴³, M.I. Ferrero⁴⁴, V. Monaco⁴⁴, R. Sacchi⁴⁴, A. Solano⁴⁴, M. Arneodo⁴⁵, M. Ruspa⁴⁵, S. Fourletov⁴⁶, J.F. Martin⁴⁶, S.K. Boutle^{47,q}, J.M. Butterworth⁴⁷, C. Gwenlan^{47,ab}, T.W. Jones⁴⁷, J.H. Loizides⁴⁷, M.R. Sutton^{47,ab}, C. Targett-Adams⁴⁷, M. Wing⁴⁷, B. Brzozowska⁴⁸, J. Ciborowski^{48,ac}, G. Grzelak⁴⁸, P. Kulinski⁴⁸, P. Luźniak^{48,ad}, J. Malka^{48,ad}, R.J. Nowak⁴⁸, J.M. Pawlak⁴⁸, T. Tymieniecka⁴⁸, A. Ukleja^{48,ae}, A.F. Żarnecki⁴⁸, M. Adamus⁴⁹, P. Plucinski^{49,af}, Y. Eisenberg⁵⁰, I. Giller⁵⁰, D. Hochman⁵⁰, U. Karshon⁵⁰, M. Rosin⁵⁰, E. Brownson⁵¹, T. Danielson⁵¹, A. Everett⁵¹, D. Kçira⁵¹, D.D. Reeder⁵¹, P. Ryan⁵¹, A.A. Savin⁵¹, W.H. Smith⁵¹, H. Wolfe⁵¹, S. Bhadra⁵², C.D. Catterall⁵², Y. Cui⁵², G. Hartner⁵², S. Menary⁵², U. Noor⁵², M. Soares⁵², J. Standage⁵², J. Whyte⁵²

¹ Argonne National Laboratory, Argonne, Illinois 60439-4815, USA^{ag}

² Andrews University, Berrien Springs, Michigan 49104-0380, USA

³ Institut für Physik der Humboldt-Universität zu Berlin, Berlin, Germany

⁴ University and INFN Bologna, Bologna, Italy^{ah}

⁵ Physikalisches Institut der Universität Bonn, Bonn, Germany^{ai}

⁶ H.H. Wills Physics Laboratory, University of Bristol, Bristol, UK^{aj}

- ⁷ Calabria University, Physics Department and INFN, Cosenza, Italy^{ah}
⁸ Chonnam National University, Kwangju, South Korea^{ak}
⁹ Jabatan Fizik, Universiti Malaya, 50603 Kuala Lumpur, Malaysia^{al}
¹⁰ Nevis Laboratories, Columbia University, Irvington on Hudson, New York 10027, USA^{am}
¹¹ The Henryk Niewodniczanski Institute of Nuclear Physics, Polish Academy of Sciences, Cracow, Poland^{an}
¹² Faculty of Physics and Applied Computer Science, AGH-University of Science and Technology, Cracow, Poland^{ao}
¹³ Department of Physics, Jagellonian University, Cracow, Poland
¹⁴ Deutsches Elektronen-Synchrotron DESY, Hamburg, Germany
¹⁵ Deutsches Elektronen-Synchrotron DESY, Zeuthen, Germany
¹⁶ University and INFN, Florence, Italy^{ah}
¹⁷ Fakultät für Physik der Universität Freiburg i.Br., Freiburg i.Br., Germany^{ai}
¹⁸ Department of Physics and Astronomy, University of Glasgow, Glasgow, UK^{aj}
¹⁹ Department of Engineering in Management and Finance, Univ. of Aegean, Mytilene, Greece
²⁰ Hamburg University, Institute of Experimental Physics, Hamburg, Germany^{ai}
²¹ Imperial College London, High Energy Nuclear Physics Group, London, UK^{aj}
²² Institute of Particle and Nuclear Studies, KEK, Tsukuba, Japan^{ap}
²³ Institute of Physics and Technology of Ministry of Education and Science of Kazakhstan, Almaty, Kazakhstan
²⁴ Kyungpook National University, Center for High Energy Physics, Daegu, South Korea^{ak}
²⁵ Institut de Physique Nucléaire, Université Catholique de Louvain, Louvain-la-Neuve, Belgium^{aq}
²⁶ Departamento de Física Teórica, Universidad Autónoma de Madrid, Madrid, Spain^{ar}
²⁷ Department of Physics, McGill University, Montréal, Québec, Canada H3A 2T8^{as}
²⁸ Meiji Gakuin University, Faculty of General Education, Yokohama, Japan^{ap}
²⁹ Moscow Engineering Physics Institute, Moscow, Russia^{at}
³⁰ Moscow State University, Institute of Nuclear Physics, Moscow, Russia^{au}
³¹ Max-Planck-Institut für Physik, München, Germany
³² NIKHEF and University of Amsterdam, Amsterdam, Netherlands^{av}
³³ Physics Department, Ohio State University, Columbus, Ohio 43210, USA^{ag}
³⁴ Department of Physics, University of Oxford, Oxford, UK^{aj}
³⁵ Dipartimento di Fisica dell'Università and INFN, Padova, Italy^{ah}
³⁶ Department of Physics, Pennsylvania State University, University Park, Pennsylvania 16802, USA^{am}
³⁷ Polytechnic University, Sagamihara, Japan^{ap}
³⁸ Dipartimento di Fisica, Università 'La Sapienza' and INFN, Rome, Italy^{ah}
³⁹ Rutherford Appleton Laboratory, Chilton, Didcot, Oxon, UK^{aj}
⁴⁰ Raymond and Beverly Sackler Faculty of Exact Sciences, School of Physics, Tel-Aviv University, Tel-Aviv, Israel^{aw}
⁴¹ Department of Physics, Tokyo Institute of Technology, Tokyo, Japan^{ap}
⁴² Department of Physics, University of Tokyo, Tokyo, Japan^{ap}
⁴³ Tokyo Metropolitan University, Department of Physics, Tokyo, Japan^{ap}
⁴⁴ Università di Torino and INFN, Torino, Italy^{ah}
⁴⁵ Università del Piemonte Orientale, Novara, and INFN, Torino, Italy^{ah}
⁴⁶ Department of Physics, University of Toronto, Toronto, Ontario, Canada M5S 1A7^{as}
⁴⁷ Physics and Astronomy Department, University College London, London, UK^{aj}
⁴⁸ Warsaw University, Institute of Experimental Physics, Warsaw, Poland
⁴⁹ Institute for Nuclear Studies, Warsaw, Poland
⁵⁰ Department of Particle Physics, Weizmann Institute, Rehovot, Israel^{ax}
⁵¹ Department of Physics, University of Wisconsin, Madison, Wisconsin 53706, USA^{ag}
⁵² Department of Physics, York University, Toronto, Ontario, Canada M3J 1P3^{as}

† deceased

Received: 26 September 2006 / Revised version: 31 January 2007 /

Published online: 15 March 2007 – © Springer-Verlag / Società Italiana di Fisica 2007

Abstract. The production of beauty quarks with a $D^{*\pm}$ and a muon in the final state has been measured with the ZEUS detector at HERA using an integrated luminosity of 114 pb^{-1} . Low transverse-momentum thresholds for the muon and D^* meson allow for a measurement of beauty production closer to the production threshold than previous measurements. The beauty signal was extracted using the charge correlations and angular distributions of the muon with respect to the D^* meson. Cross sections for photoproduction and deep inelastic scattering are somewhat higher than, but compatible with, next-to-leading-order QCD predictions, and compatible with other measurements.

^a supported by DESY, Germany

1 Introduction

The production of beauty quarks in ep collisions at HERA is a stringent test for perturbative quantum chromodynamics (QCD) since the large b -quark mass ($m_b \sim 5$ GeV) provides a hard scale that should ensure reliable predictions. For b -quark transverse momenta comparable to the

b -quark mass, next-to-leading-order (NLO) QCD calculations in which the b quarks are generated dynamically are expected to provide accurate predictions [1–7].

The beauty-production cross section has been measured in $p\bar{p}$ collisions at the $Spp\bar{S}$ [8–11] and Tevatron colliders [12–21], in $\gamma\gamma$ interactions at LEP [22, 23], in fixed-target πN [24, 25] and pN [26–28] experiments, and in ep collisions at HERA [29–39]. While most results, including recent results from the Tevatron, are in agreement with QCD predictions, some, in particular those from LEP, show large discrepancies.

This paper reports a measurement of beauty production via the reaction $ep \rightarrow ebbX \rightarrow eD^*\mu X'$ using the ZEUS detector at HERA. This reaction offers the advantage of providing a data sample enriched in b quarks and with strongly suppressed backgrounds from other processes, which allows low- p_T threshold cuts to be applied. This analysis therefore yields a measurement of beauty production closer to the production threshold than previous HERA measurements based on leptons and/or jets with high transverse momentum [29–38]. A similar measurement has been performed by the H1 collaboration [39].

Of particular interest are events in which the muon and D^* originate from the same parent B meson (Fig. 1a), e.g. $B^0 \rightarrow D^{*-}\mu^+\nu_\mu$. These yield unlike-sign D^* -muon pairs produced in the same detector hemisphere. Due to the partial reconstruction (e.g. a missing neutrino) the invariant mass is constrained to lie below the B -meson mass. Another important contribution arises from charm-pair production, where one charm quark fragments into a D^* and the other decays into a muon (Fig. 1b). This again

^b also affiliated with University College London, UK
^c also at University of Hamburg, Germany, Alexander von Humboldt Fellow
^d self-employed
^e retired
^f now at Univ. of Wuppertal, Germany
^g formerly U. Meyer
^h supported by Chonnam National University in 2005
ⁱ supported by a scholarship of the World Laboratory Björn Wiik Research Project
^j supported by the research grant no. 1 P03B 04529 (2005–2008)
^k now at DESY group FEB, Hamburg, Germany
^l also at Institut of Theoretical and Experimental Physics, Moscow, Russia
^m also at INP, Cracow, Poland
ⁿ on leave of absence from FPACS, AGH-UST, Cracow, Poland
^o e-mail: gallo@mail.desy.de
^p partly supported by Moscow State University, Russia
^q also affiliated with DESY
^r now at CERN, Geneva, Switzerland
^s also at University of Tokyo, Japan
^t Ramón y Cajal Fellow
^u partly supported by Russian Foundation for Basic Research grant no. 05-02-39028-NSFC-a
^v EU Marie Curie Fellow
^w partially supported by Warsaw University, Poland
^x also at Max Planck Institute, Munich, Germany, Alexander von Humboldt Research Award
^y now at KEK, Tsukuba, Japan
^z now at Nagoya University, Japan
^{aa} Department of Radiological Science
^{ab} PPARC Advanced fellow
^{ac} also at Łódź University, Poland
^{ad} Łódź University, Poland
^{ae} supported by the Polish Ministry for Education and Science grant no. 1 P03B 12629
^{af} supported by the Polish Ministry for Education and Science grant no. 1 P03B 14129
^{ag} supported by the US Department of Energy
^{ah} supported by the Italian National Institute for Nuclear Physics (INFN)
^{ai} supported by the German Federal Ministry for Education and Research (BMBF), under contract numbers HZ1GUA 2, HZ1GUB 0, HZ1PDA 5, HZ1VFA 5
^{aj} supported by the Particle Physics and Astronomy Research Council, UK
^{ak} supported by the Korean Ministry of Education and Korea Science and Engineering Foundation
^{al} supported by the Malaysian Ministry of Science, Technology and Innovation/Akademi Sains Malaysia grant SAGA 66-02-03-0048

^{am} supported by the US National Science Foundation
^{an} supported by the Polish State Committee for Scientific Research, grant no. 620/E-77/SPB/DESY/P-03/DZ 117/2003-2005 and grant no. 1P03B07427/2004-2006
^{ao} supported by the Polish Ministry of Science and Higher Education
^{ap} supported by the Japanese Ministry of Education, Culture, Sports, Science and Technology (MEXT) and its grants for Scientific Research
^{aq} supported by FNRS and its associated funds (IISN and FRIA) and by an Inter-University Attraction Poles Programme subsidised by the Belgian Federal Science Policy Office
^{ar} supported by the Spanish Ministry of Education and Science through funds provided by CICYT
^{as} supported by the Natural Sciences and Engineering Research Council of Canada (NSERC)
^{at} partially supported by the German Federal Ministry for Education and Research (BMBF)
^{au} supported by RF Presidential grant N 1685.2003.2 for the leading scientific schools and by the Russian Ministry of Education and Science through its grant for Scientific Research on High Energy Physics
^{av} supported by the Netherlands Foundation for Research on Matter (FOM)
^{aw} supported by the German–Israeli Foundation and the Israel Science Foundation
^{ax} supported in part by the MINERVA Gesellschaft für Forschung GmbH, the Israel Science Foundation (grant no. 293/02-11.2) and the U.S.–Israel Binational Science Foundation

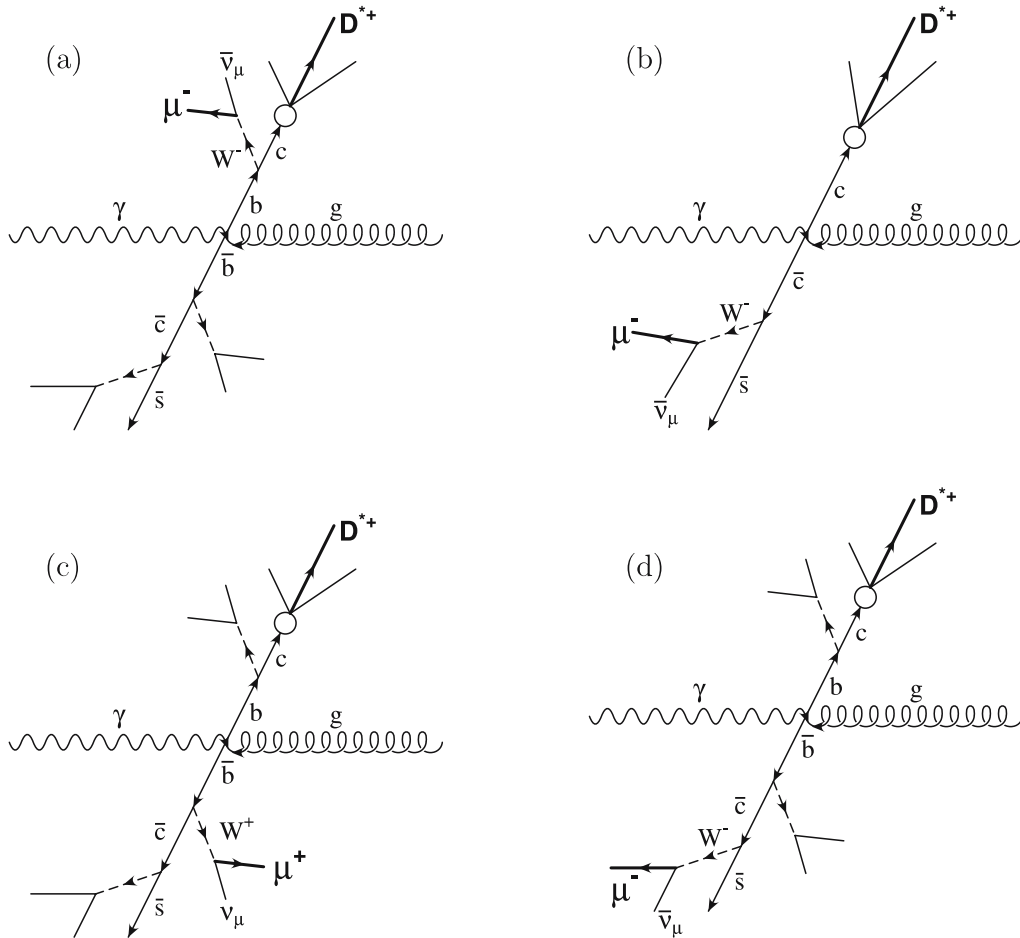


Fig. 1. Processes leading to final states $D^* \mu$

yields unlike-sign D^* -muon pairs, but with the D^* and the muon produced predominantly in opposite hemispheres. In addition, beauty-pair production in which the D^* and muon originate from different beauty quarks can yield both like- and unlike-sign D^* -muon combinations, depending on whether the muon is from the decay of the primary beauty quark (Fig. 1c) or from a secondary charm quark (Fig. 1d), and whether $B^0 - \bar{B}^0$ mixing has occurred.

Background contributions to both like- and unlike-sign combinations include events with either fake D^* mesons, originating from combinatorial background, or fake muons. In this analysis, the signal is extracted from the unlike-sign sample, while the like-sign sample is used as a cross check.

Cross sections are extracted separately for the photoproduction (γp , photon virtuality $Q^2 \lesssim 1 \text{ GeV}^2$) and deep inelastic scattering (DIS, $Q^2 \gtrsim 1 \text{ GeV}^2$) regimes, as well as for the entire range in Q^2 , which includes the kinematic region in which these two event classes cannot easily be distinguished.

2 Experimental set-up

The data sample used in this analysis corresponds to an integrated luminosity $\mathcal{L} = 114.1 \pm 2.3 \text{ pb}^{-1}$, collected by the

ZEUS detector in the years 1996–2000. During the 1996–1997 data taking, HERA provided collisions between an electron¹ beam of $E_e = 27.5 \text{ GeV}$ and a proton beam of $E_p = 820 \text{ GeV}$, corresponding to a centre-of-mass energy $\sqrt{s} = 300 \text{ GeV}$ ($\mathcal{L}_{300} = 38.0 \pm 0.6 \text{ pb}^{-1}$). In the years 1998–2000, the proton-beam energy was $E_p = 920 \text{ GeV}$, corresponding to $\sqrt{s} = 318 \text{ GeV}$ ($\mathcal{L}_{318} = 76.1 \pm 1.7 \text{ pb}^{-1}$).

A detailed description of the ZEUS detector can be found elsewhere [40]. A brief outline of the components that are most relevant for this analysis is given below.

Charged particles are tracked in the central tracking detector (CTD) [41–43], which operates in a magnetic field of 1.43 T, provided by a thin superconducting coil. The CTD consists of 72 cylindrical drift chamber layers, organized in nine superlayers covering the polar-angle² region $15^\circ < \theta < 164^\circ$. The transverse-momentum resolution for full-length

¹ Electrons and positrons are not distinguished in this paper and are both referred to as electrons.

² The ZEUS coordinate system is a right-handed Cartesian system, with the Z axis pointing in the proton-beam direction, referred to as the “forward direction”, and the X axis pointing left towards the centre of HERA. The coordinate origin is at the nominal interaction point. The pseudorapidity is defined as $\eta = -\ln\left(\tan\frac{\theta}{2}\right)$, where the polar angle, θ , is measured with respect to the proton-beam direction.

tracks is $\sigma(p_T)/p_T = 0.0058p_T \oplus 0.0065 \oplus 0.0014/p_T$, with p_T in GeV.

The high-resolution uranium-scintillator calorimeter (CAL) [44–47] consists of three parts: the forward (FCAL), the barrel (BCAL) and the rear (RCAL) calorimeters. Each part is subdivided transversely into towers and longitudinally into one electromagnetic section and either one (in RCAL) or two (in BCAL and FCAL) hadronic sections. The smallest subdivision of the calorimeter is called a cell. The CAL energy resolutions, as measured under test-beam conditions, are $\sigma(E)/E = 0.18/\sqrt{E}$ for electrons and $\sigma(E)/E = 0.35/\sqrt{E}$ for hadrons, with E in GeV.

The position of electrons scattered at small angles to the electron beam direction was measured using the small-angle rear tracking detector (SRTD) [48, 49]. The SRTD is attached to the front face of the RCAL and consists of two planes of scintillator strips, arranged orthogonally. The strips are 1 cm wide and 0.5 cm thick.

The muon system consists of rear, barrel (R/B-MUON) [50] and forward (FMUON) [40] tracking detectors. The B/RMUON consists of limited-streamer tube chambers placed behind the BCAL (RCAL), inside and outside a magnetized iron yoke surrounding the CAL. These chambers cover polar angles from 34° to 135° and from 135° to 171° , respectively.

The luminosity was measured using the bremsstrahlung process $ep \rightarrow ep\gamma$. The resulting small-angle energetic photons were measured by the luminosity monitor [51–53], a lead-scintillator calorimeter placed in the HERA tunnel at $Z = -107$ m.

3 Data selection

The data were selected online via a three-level trigger system through a combination of three different trigger chains:

- a muon reaching the inner B/RMUON chambers and matched to a minimum ionizing energy deposit in the CAL or any muon reaching the outer B/RMUON chambers or
- a D^* candidate [54] or
- a scattered-electron candidate in the CAL [38]. In part of the data taking, the cuts on the electron candidate were relaxed if a muon in the inner B/RMUON chambers was detected.

Due to this redundancy, the trigger efficiency for beauty events was high, $94 \pm 3\%$ for the inclusive study, and $98 \pm 2\%$ for the DIS selection.

Muons were reconstructed offline using the following procedure: a track was found in the inner B/RMUON chambers, then a match in position and angle to a CTD track was required. In the bottom region of the detector, where there are no inner chambers, the outer chambers were used instead. If a match was found to both inner and outer chambers, a momentum-matching criterion was added.

The angular coverage of the B/RMUON and of the track requirements in the CTD restrict the muon accept-

ance to the pseudorapidity region

$$-1.75 < \eta^\mu < 1.3. \quad (1)$$

A cut on the muon transverse momentum

$$p_T^\mu > 1.4 \text{ GeV} \quad (2)$$

was applied, reflecting the requirement that the muon reaches the inner muon chambers in the barrel region. In order to have a uniform kinematic acceptance, this cut was also applied in the rear region.

D^* candidates were reconstructed in the $D^{*+} \rightarrow D^0(\rightarrow K^-\pi^+)\pi_s^+$ decay channel (+c.c.) making use of the ΔM ($\equiv M(K\pi\pi_s) - M(K\pi)$) technique described in previous publications [54] with the following cuts:

$$\begin{aligned} D^0 \text{ mass} & 1.81 < M(K\pi) < 1.92 \text{ GeV}; \\ D^* - D^0 \text{ mass difference} & 0.1435 < \Delta M < 0.1475 \text{ GeV}; \\ D^* \text{ transverse momentum} & p_T^{D^*} > 1.9 \text{ GeV}; \\ D^* \text{ pseudorapidity} & |\eta^{D^*}| < 1.5; \\ K, \pi \text{ transverse momentum} & p_T^{K,\pi} > 0.5 \text{ GeV}; \\ \text{slow pion} & p_T^{\pi_s} > 0.125 \text{ GeV}. \end{aligned} \quad (3)$$

To allow the background to the D^* signal to be determined, D^0 candidates with wrong-charge combinations, in which both tracks forming the D^0 candidates have the same charge and the third track has the opposite charge, were also retained.

The hadronic system was reconstructed from the calorimeter information and the reconstructed vertex. A four-momentum $(p_X^i, p_Y^i, p_Z^i, E^i)$ was assigned to each calorimeter cell. Global hadronic variables were reconstructed by summing over these cells. In the case of identified DIS events (see below), the scattered-electron candidates were excluded from this sum. The inelasticity y was reconstructed from the Jacquet–Blondel estimator $y_{JB} = (E - P_Z)/2E_e$ [55], where $E - P_Z = \sum_i (E^i - p_Z^i)$ and the sum runs over all cells. In the case of DIS events, the alternative value $y_e = 1 - \frac{E'_e}{2E_e}(1 - \cos\theta_e)$ as well as the photon virtuality Q^2 were obtained from the energy E'_e and scattering angle θ_e of the final-state electron candidate [38]. A sample of events with one muon and one D^* candidate was selected by requiring:

- ≥ 1 muon in the muon chamber regions defined by (1) and (2);
- ≥ 1 D^* candidate in the D^* acceptance region defined by (3);
- the muon candidate track is not one of the three D^* candidate tracks, eliminating backgrounds from semileptonic D^0 decays;
- the $D^* \mu$ system carries a significant fraction of the total transverse energy of the event, $p_T^{D^* \mu}/E_T > 0.14$, where E_T is the transverse energy measured by the CAL outside a cone of 10° around the proton-beam direction to exclude the proton remnant, and $p_T^{D^* \mu}$ is the transverse momentum of the $D^* \mu$ system, reducing combinatorial D^* background;

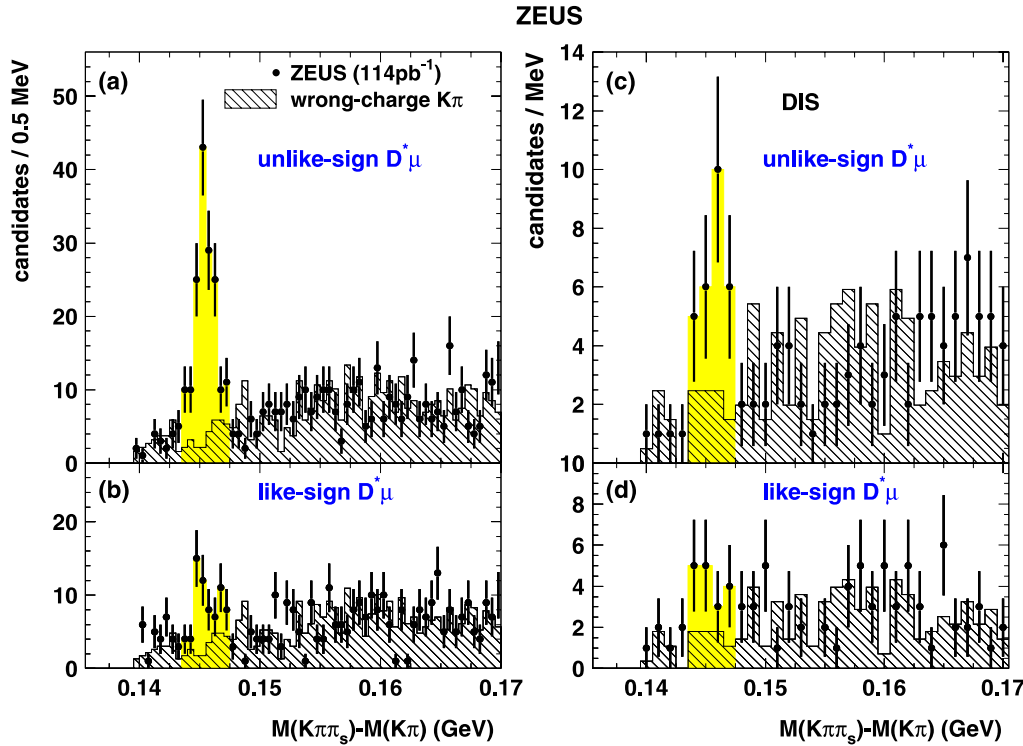


Fig. 2. Distribution of ΔM for data (*full circles*) and combinatorial background (*hatched histogram*) for **a** inclusive unlike-sign, **b** inclusive like-sign, **c** DIS unlike-sign and **d** DIS like-sign muon- D^* combinations. The D^* signal region is indicated by the *shaded area*

– a reconstructed vertex compatible with the nominal interaction point, suppressing non- ep background.

After this selection, a sample of 232 events remained. The resulting ΔM distributions for the like and unlike $D^* \mu$ charge combinations, before the ΔM cut, are shown in Fig. 2a and b.

A subsample of photoproduction events was selected by requiring:

- no scattered-electron candidate found in the CAL;
- $E - P_Z < 34$ GeV;

retaining 81% of the inclusive sample. After the unfolding of the detector response, these cuts correspond to an effective cut $Q^2 < 1$ GeV² and $0.05 < y < 0.85$. The lower limit on y arises from the interplay between the b -quark mass and the acceptance in rapidity.

Alternatively, a clean DIS sample was obtained by applying the following additional conditions [38]:

- a reconstructed electron with energy $E'_e > 10$ GeV;
- $Q^2 > 2$ GeV²;
- inelasticity $y_{JB} > 0.05$ and $y_e < 0.7$;
- $40 < E - P_Z < 60$ GeV;
- the electron hits the rear calorimeter outside a rectangle of $|X| < 13$ cm and $|Y| < 7$ cm.

These cuts correspond to an effective cut $Q^2 > 2$ GeV² and $0.05 < y < 0.7$. For this sample, which contains less combinatorial background, the D^* cuts were relaxed to

$$\begin{aligned}
 p_T^{D^*} &> 1.5 \text{ GeV}; \\
 p_T^{K,\pi} &> 0.4 \text{ GeV}; \\
 p_T^{\pi_s} &> 0.12 \text{ GeV};
 \end{aligned}
 \tag{4}$$

and the cut on $p_T^{D^* \mu} / E_T$ was dropped. All other cuts on the D^* and the muon remained unchanged. A sample of 44 events was obtained. The resulting ΔM distributions for the like and unlike $D^* \mu$ charge combinations are shown in Fig. 2c and d.

4 Backgrounds and event simulation

Several contributions to the selected data sample were evaluated:

- the signal from beauty decays;
- the background from fake D^* combinations;
- the $D^* \mu$ background from charm decays;
- the background from fake or non-prompt muons with a real D^* from charm.

For the signal from beauty and charm production, Monte Carlo (MC) simulations were performed using the PYTHIA [56], RAPGAP [57] and HERWIG [58] generators. These simulations are based on leading-order matrix elements complemented by parton showers to obtain higher-order topologies. The direct photon-gluon fusion process ($\gamma g \rightarrow Q\bar{Q}$, $Q = b, c$), flavour excitation in the resolved photon and proton (e.g. $Qg \rightarrow Qg$, $\gamma Q \rightarrow Qg$), and hadron-like resolved photon processes ($gg \rightarrow Q\bar{Q}$) were included. Gluon splitting into heavy flavours ($g \rightarrow Q\bar{Q}$) in events with only light quarks in the hard scattering was not included in the simulations; this contribution is, however, expected to be small [59]. For all generated events, the ZEUS detector response was simulated in detail using a programme based on GEANT 3.21 [60].

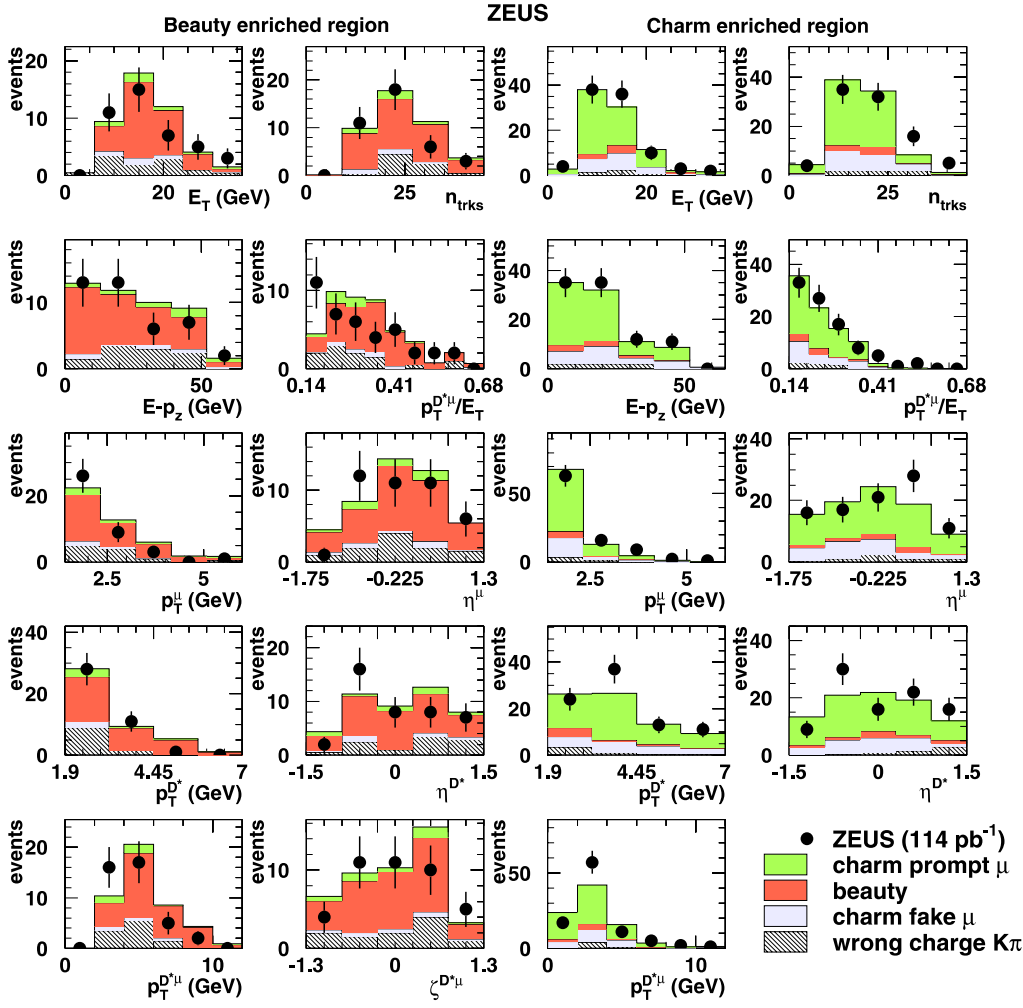


Fig. 3. Distributions of variables used in the event selection or relevant for the event kinematics, for the unlike-sign inclusive sample after all cuts. All variables are defined in the text except n_{trks} (total number of tracks) and $\zeta^{D^*\mu}$ (rapidity of the $D^*\mu$ system). The distributions are shown separately for the beauty- and charm-enriched regions as defined in Sect. 5. The beauty, charm, fake-muon and wrong-charge $K\pi$ background distributions are indicated by different shading styles, and they are normalised to the fractions determined later in the analysis

The number of background events under the D^* mass peaks (fake D^*) was estimated using the wrong-charge $K\pi$ combinations combining the like- and unlike-sign samples. This was found to minimize the bias due to charge correlations [59]. Wrong-charge combinations were normalised to the data outside the D^* peak in the side-band $0.15 < \Delta M < 0.17$ GeV, separately for the like-sign and unlike-sign $D^*\mu$ sample, as shown in Fig. 2. Dedicated studies [59] performed by selecting data on the D^* side-band showed that this procedure correctly reproduces the shape and normalisation of the fake- D^* background for the relevant variables used in the analysis.

Fake muons can be produced by hadron showers leaking from the back of the calorimeter or by charged hadrons traversing the entire calorimeter without interaction. In addition, low-momentum muons can originate from in-flight decays of pions and kaons. It is also possible for tracks reconstructed in the central tracker to be wrongly associated to a signal from a real muon in the muon chambers. A dedicated study [59] based on pions from K^0 decays, protons from Λ decays, and kaons from ϕ and D^* decays, showed that the detector simulation reproduced these backgrounds reasonably well. The fake-muon probability for the $K^0 \rightarrow \pi^+\pi^-$ sample is about 0.2%. Most fake muons are as-

sociated with fake D^* candidates, and therefore they are accounted for in the fake- D^* background estimated directly from the data. Fake muons associated with a real D^* are included in the charm and beauty MC samples.

Distributions of variables used in the event selection or relevant for the event kinematics, for the unlike-sign inclusive sample, are compared to the expectations from these simulations in Fig. 3, separately for the beauty- and charm-enriched regions defined in Sect. 5. Agreement with expectations is obtained, apart from some possible deviations in the $p_T^{D^*\mu}$ and $p_T^{D^*\mu}/E_T$ distributions in the beauty-enriched region, which are accounted for in the systematic uncertainties (Sect. 7).

5 Signal extraction

In this section, the signal-extraction procedure is described for the inclusive sample. The γp subsample and the DIS sample were treated in an analogous way.

Figure 4a and b show the distribution of the angular difference $\Delta R = \sqrt{\Delta\phi^2 + \Delta\eta^2}$ between the D^* and the muon, where ϕ is the azimuthal angle, for events passing

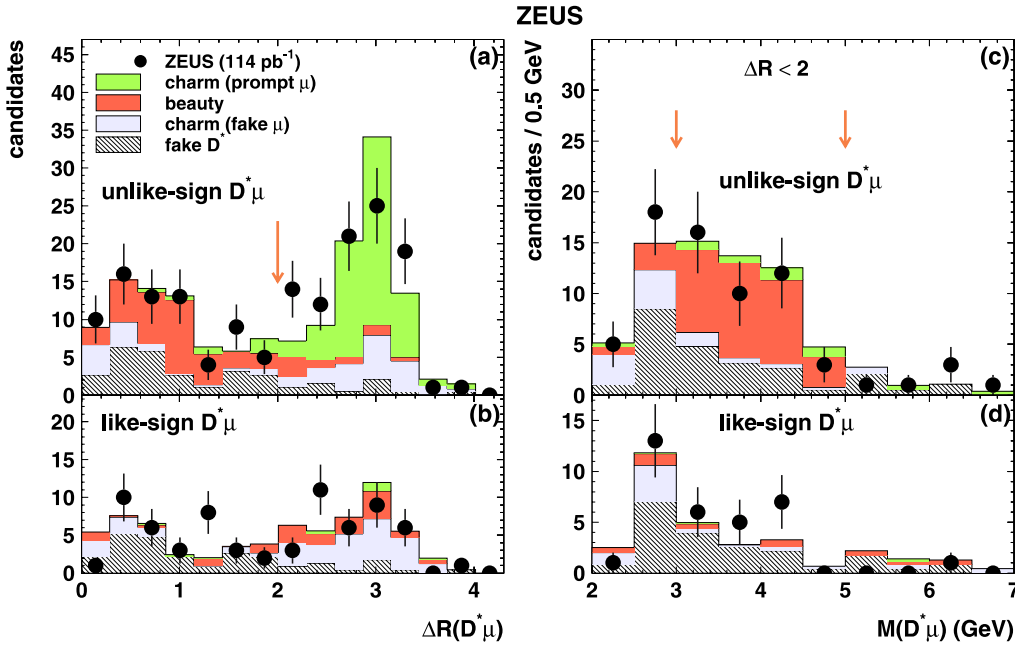


Fig. 4. Distribution of **a**, **b** $\Delta R(D^* \mu)$ and **c**, **d** $M(D^* \mu)$ for inclusive data (full circles), beauty and charm signal, fake- μ and fake- D^* backgrounds. The latter are distinguished by different shading styles. Unlike-sign and like-sign $D^* \mu$ combinations are shown separately. Cuts described in the text are indicated by the arrows. The relative contributions of charm and beauty are determined by the fit to the ΔR distribution

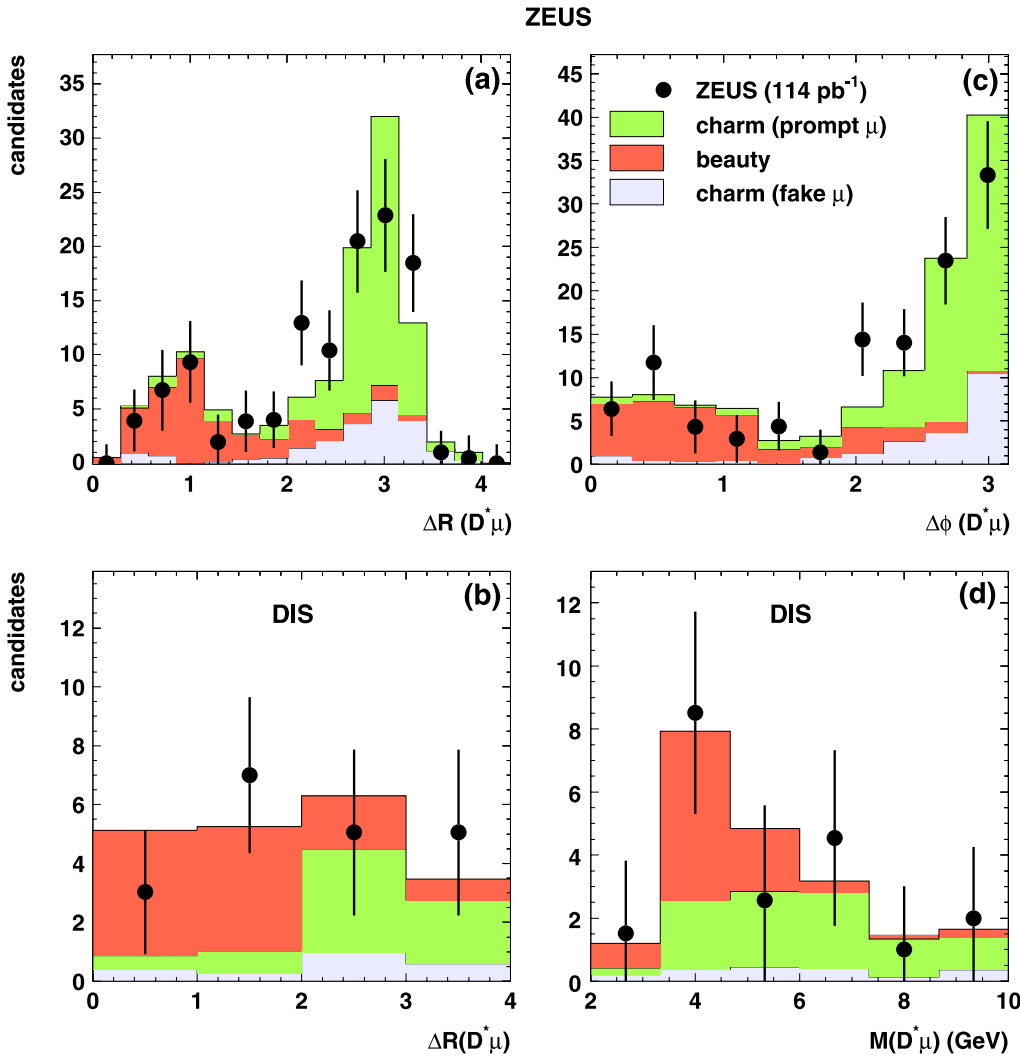


Fig. 5. Distributions of **a** $\Delta R(D^* \mu)$, **c** $\Delta \phi(D^* \mu)$ for unlike-sign events in the inclusive sample, **b** $\Delta R(D^* \mu)$ and **d** $M(D^* \mu)$ for unlike-sign events in the DIS sample after subtraction of the fake- D^* background. Data points (full circles) are shown together with the contributions from beauty and charm, as determined in the fit. The fake-muon contribution from charm is shown separately, but fitted together with the charm contribution

Table 1. Composition of the final $D^*\mu$ event samples (number of events) as determined from the fit to the ΔR distribution

Sample	Cuts	Data	Beauty	Charm		Fake D^*
				prompt μ	fake μ	
				Inclusive sample		
unlike sign	$\Delta R < 2, 3 < M < 5$ GeV	41	28.8	3.6	2.5	11.2
	$\Delta R > 2$	93	6.5	56.5	18.4	6.4
like sign	$\Delta R < 2, 3 < M < 5$ GeV	18	1.6	0.7	1.3	9.2
	$\Delta R > 2$	36	11.1	2.0	21.2	5.2
				γp		
unlike sign	$\Delta R < 2, 3 < M < 5$ GeV	31	23.6	1.2	1.6	8.3
	$\Delta R > 2$	79	6.2	48.8	14.0	6.2
like sign	$\Delta R < 2, 3 < M < 5$ GeV	14	1.5	0.6	0.4	6.9
	$\Delta R > 2$	28	9.1	1.9	17.1	5.2
				DIS		
unlike sign	$\Delta R < 2, 3 < M < 5$ GeV	11	8.1	1.6	0.5	1.0
	$\Delta R > 2$	14	3.2	6.1	1.2	3.9
like sign	$\Delta R < 2, 3 < M < 5$ GeV	3	1.2	0.1	0.5	0.3
	$\Delta R > 2$	10	5.0	0.2	2.6	1.2

all selections, including the ΔM cut. The distributions are shown separately for like- and unlike-sign $D^*\mu$ events. The expected signal and background distributions, normalised to the fractions determined later in the analysis and described below, are also indicated. For unlike-sign events, the region $\Delta R > 2$, which mainly corresponds to the back-to-back configuration, is clearly dominated by events from charm. Indications that the simulated distribution might be more sharply peaked than the data turned out to have little influence on the determination of the beauty fraction. In contrast, the region $\Delta R < 2$ is enriched in beauty events, in which the D^* and muon originate mainly from decays of the same parent B hadron. This is illustrated further in the $D^*\mu$ invariant-mass distribution (Fig. 4c and d) for events in the beauty-enriched region ($\Delta R < 2$). A peak with an upper edge close to 5 GeV, which can be attributed to the partial reconstruction of the decaying B meson, is clearly visible. A comparison with the like-sign sample shows that the low-mass edge of this peak is dominated by background. An invariant-mass cut of $3 \text{ GeV} < M(D^*\mu) < 5 \text{ GeV}$ was therefore applied to the $\Delta R < 2$ subsample.

After this additional cut, and after statistical subtraction of the fake- D^* background, the contributions of charm and beauty were determined by a two-component fit to the ΔR or $\Delta\phi$ distributions, shown in Fig. 5a and c. The fake-muon background with a real D^* from charm, which is treated as part of the charm component, is shown separately. The small fraction of fake muons from beauty was included in the beauty component. The fit result for the fraction of beauty events in the final inclusive sample shown in Fig. 5a and c, using the shapes predicted by PYTHIA, is:

- $f_b = 0.307 \pm 0.064$ (stat.) for the ΔR and
- $f_b = 0.290 \pm 0.062$ (stat.) for the $\Delta\phi$ distribution.

The ΔR result was chosen as the reference, and the $\Delta\phi$ result used as a systematic check. With these fitted fractions, the breakdown into the corresponding number of beauty,

charm, and fake-muon candidates in each subsample is given in Table 1. In the unlike-sign part, the beauty and charm contributions are well separated, with only small cross-contaminations. The normalisation of the beauty and charm contributions in Fig. 4 already reflects these fitted fractions. Agreement is seen, also in the like-sign part, which was not included in the fit.

The results from the application of the same procedure to the γp subsample are also shown in Table 1. The analogous results for the DIS sample are shown in Fig. 5b and d. The $\Delta\phi$ distribution gives less discrimination in this case, due to the transverse boost from the exchanged virtual photon. Therefore, the $M(D^*\mu)$ distribution was used. The fitted beauty fractions in the DIS sample, using the shapes predicted by RAPGAP, are

- $f_b = 0.55 \pm 0.25$ (stat.) for the ΔR and
- $f_b = 0.43 \pm 0.30$ (stat.) for the $M(D^*\mu)$ distribution.

Again, the ΔR result is chosen as the reference, and the other as a cross check. The breakdown into different event categories is shown in Table 1. The acceptance corrections for the cross sections, which will be presented in Sect. 8, were evaluated using PYTHIA for $Q^2 < 1 \text{ GeV}^2$, RAPGAP for $Q^2 > 1 \text{ GeV}^2$, and HERWIG as a systematic check.

6 Theoretical predictions and uncertainties

For direct comparisons with QCD, next-to-leading-order predictions were used. Calculations in which b quarks are treated as massless particles [61–63] are not applicable in this kinematic range, while calculations based on alternative parton-evolution schemes [64–67] do not yet exist with full NLO implementation. Fixed-order NLO calculations with massive b quarks should yield accurate predictions. Different types of such predictions were evaluated.

The FMNR program [1] evaluates cross sections for next-to-leading-order beauty production in γp collisions

in the fixed-order massive approach, for both point-like and hadron-like photon coupling to the heavy quarks. The parton-density functions used were CTEQ5M [68] for the proton and GRV-G-HO [69] for the photon. The renormalisation and factorisation scales μ were chosen to be equal and parametrised by $\mu_0 = \sqrt{p_T^2 + m_b^2}$, where p_T^2 is the average of the squared transverse momentum of the two emerging b quarks and $m_b = 4.75$ GeV. An estimate of the theoretical uncertainty was obtained by simultaneously varying $4.5 < m_b < 5.0$ GeV and $\mu_0/2 < \mu < 2\mu_0$ such that the uncertainty was maximised. Typical uncertainties resulting from this procedure (e.g. for the $b\bar{b}$ total cross section) are +40% and -25%. Variations of the parton densities led to uncertainties which were much smaller than the uncertainties related to mass and scale variations. They were therefore neglected.

Predictions at the level of visible $D^* \mu$ final states are needed in addition to those at parton level. The FMNR program provides a framework to fragment b quarks into B hadrons and to simulate the decay of these hadrons by interfacing them to appropriately chosen decay spectra. However, decays to complex final states, such as a D^* and μ from the same B hadron with cuts on both particles, cannot easily be implemented in this scheme. A straightforward interface of the parton-level events produced by FMNR to MC-like fragmentation and decay chains is also impracticable, since these events have positive and negative weights spanning more than eight orders of magnitude, making such an approach extremely inefficient.

These difficulties were overcome in a two-step process. In the first step, two or more FMNR parton-level events with large positive and negative weights and similar topology were combined into events with much smaller weights by averaging the parton momentum vectors [70]. Events were considered to have similar topology if the differences in transverse momentum, rapidity and azimuthal angle of the b quarks were less than user cut values that reflect the detector resolution. Furthermore, events with small weights were sampled with a probability proportional to their weight. In this way, the weight range was reduced to about two orders of magnitude. It was explicitly checked that this procedure preserves the NLO accuracy for the relevant cross sections at parton level (e.g. b quark p_T and angular distributions).

In the second step, these parton-level events were interfaced to the PYTHIA/JETSET [71] fragmentation and decay chain, making use of the full decay tables and decay kinematics implemented in PYTHIA 6.2. Therefore, non-dominant complex decays, such as $B \rightarrow D^* D$ followed by $D \rightarrow \mu X$, or muons produced through intermediate J/ψ or τ states, were automatically included. The initial-state partons were allowed to have intrinsic k_T (typically ~ 300 MeV) as implemented in PYTHIA. This has a negligible effect on the resulting cross sections ($\sim 1\%$). Parton showering was not included in order to avoid double counting of higher-order contributions.³

³ The MC@NLO approach [72, 73], which allows for the combination of NLO matrix elements with parton showers, is not yet available for ep interactions.

Fragmentation of b quarks close to production threshold is non-trivial. The details of the threshold treatment were found to be much more important than the choice of a particular fragmentation function. The Peterson formula [74] with $\epsilon = 0.0035$ was used. Three approaches were considered.

- independent fragmentation as implemented in PYTHIA [71]. The use of this quite old model was motivated by the fact that FMNR does not provide colour connections on an event-by-event basis;
- fragmentation in the Lund string model [75–77], again as implemented in PYTHIA. For this purpose, reasonable colour connections were assigned to each event;
- the independent fragmentation scheme provided within the FMNR framework, rescaling the B -hadron momentum to a fraction of the b -quark momentum according to the Peterson formula, which is a somewhat crude approximation at threshold.

The second option was used for all central predictions. The first option was used to obtain the lower systematic error (typically -5%). The third option could not be applied directly, since it does not provide cross-section predictions for correlated final states from the same b quark, as needed here. Instead, it was applied to a cross section in which the final-state correlations originate from different b quarks only, which is more easily calculable in this scheme. The results were used to evaluate a generic upper systematic error of +15% on the fragmentation procedure close to b production threshold. The effect of a variation of the Peterson parameter ϵ in the range 0.0023 to 0.0045 was found to yield uncertainties that were much smaller than the uncertainties due to the different fragmentation procedures. It was therefore neglected.

The branching fractions were corrected to correspond to those obtained from the Particle Data Group [78], as listed in Table 2. Branching fraction uncertainties re-

Table 2. Branching fractions assumed for cross-section determinations. The indirect contributions include cascade decays into muons via charm, anticharm, τ^\pm and J/ψ . The values in the table are given before the inclusion of the effect of $B^0-\bar{B}^0$ mixing (mixing parameter $\chi = 0.1257 \pm 0.0042$) [78]

channel	branching fraction w/o $B^0-\bar{B}^0$ mixing
$b \rightarrow D^{*\pm}$ inclusive	17.3 ± 2.0 % 86 ± 3 % D^{*+} , 14 ± 3 % D^{*-}
$b \rightarrow \mu^-$ direct	10.95 ± 0.27 %
$b \rightarrow \mu^+$ indirect	8.27 ± 0.40 %
$b \rightarrow \mu^-$ indirect	2.21 ± 0.50 %
all $b \rightarrow \mu^\pm$	21.43 ± 0.70 %
$b\bar{b} \rightarrow D^{*\pm} \mu^\pm$ (diff. bs)	4.34 ± 0.92 %
$b\bar{b} \rightarrow D^{*\pm} \mu^\mp$ (diff. bs)	3.08 ± 0.60 %
$b \rightarrow D^{*+} \mu^-$ direct	2.75 ± 0.19 %
$b \rightarrow D^{*\pm} \mu^\mp$ indirect	1.09 ± 0.27 %
all $b \rightarrow D^{*\pm} \mu^\mp$	3.84 ± 0.33 %

sulted in uncertainties on the $D^* \mu$ cross section of typically $\pm 12\%$.

In principle, FMNR predictions are only valid for the photoproduction regime. The Weizsäcker–Williams approximation with an effective Q_{max}^2 cutoff of 25 GeV^2 ($\sim m_b^2$) [79–81] was used to include the $\sim 15\%$ DIS contribution to the combined cross section.

Alternatively, the DIS part can be calculated using the NLO predictions from HVQDIS [4–7]. Only point-like contributions are included in this prediction. The parton-density function used was CTEQ5F4 [68]. The renormalisation and factorisation scales μ were chosen to be equal and parametrised by $\mu_0 = \sqrt{Q^2 + m_b^2}$. Mass and scales were varied as for FMNR. A scheme for the calculation of visible cross sections for correlated final states, corresponding to the FMNR \otimes PYTHIA interface described above, was not available. Therefore, cross-section comparisons in DIS are limited to the parton level.

7 Systematic uncertainties

The main experimental uncertainties are described below, in order of importance. Numbers in parentheses are quoted for the inclusive selection. Uncertainties for the γp results are also quoted when they differ significantly from the inclusive results. For the DIS sample, the statistics were often too small to derive meaningful systematic errors. The errors from the inclusive sample were used instead.

- **Simulation of $p_{\text{T}}^{D^* \mu}$.** The largest error arises from the observation that the muon and D^* p_{T} spectra in the b signal region of the data ($\Delta R(D^* \mu) < 2$, $3 < M(D^* \mu) < 5 \text{ GeV}$) appear to be somewhat softer than predicted by the Monte Carlo simulations (Fig. 3). The differences are concentrated at small values of $p_{\text{T}}^{D^* \mu}/E_{\text{T}}$. Since the corresponding spectra are well reproduced in the charm region with larger statistics, this cannot be attributed to problems with the muon or D^* reconstruction. There are several ways to interpret these differences.
 - a) They are statistical fluctuations. This assumption leads to the central result reported;
 - b) The signal distribution is significantly softer than predicted by QCD. Due to the rising efficiency as a function of p_{T}^b , this would change the efficiency calculation for the measurement of the visible cross section. To evaluate this possibility, the MC $p_{\text{T}}^{D^* \mu}$ (true level) distribution in the signal region was reweighted to be compatible at the 1σ level with the measured $p_{\text{T}}^{D^* \mu}$ spectrum of the inclusive sample (Fig. 3) (+14%);
 - c) There is an additional unknown background contribution at low p_{T} , which occurs only in the beauty-enriched region. There is no indication that this is the case. Nevertheless, to account for this possibility, the $p_{\text{T}}^{D^* \mu}/E_{\text{T}}$ cut was tightened from 0.14 to 0.2, which removes most of the differences (Fig. 3) (–33% for inclusive, –18% for γp selection).

- **Branching fractions.** The beauty-enriched region, which dominates the fit result, is mainly populated by events in which the D^* and μ originate from the same b . The rate of these events depends on branching fractions different from those relevant to the charm-enriched region, in which the D^* and μ originate from different b quarks. Variation of these branching fractions, within the uncertainties quoted in Table 2, therefore affects the shape of the beauty contribution and the fitted beauty fraction ($\pm 8\%$).
- **Fragmentation and parton showering.** The HERWIG MC uses a fragmentation model different from that of PYTHIA and RAPGAP. It also yields different $b\bar{b}$ correlations from direct/resolved contributions and parton showering. This leads to differences in the acceptance, and in the fitted beauty fraction (+5/–8%).
- **Signal-extraction procedure.** In addition to statistical fluctuations, different ways to fit the data can yield systematic differences due to binning effects and different systematics for different variables, e.g. imperfections in the shape of the MC distributions. To check the error from this effect, the cross sections were evaluated using different procedures: fits to $\Delta R(D^* \mu)$, $\Delta \phi(D^* \mu)$, $M(D^* \mu)$, and simple event counting. In all cases the differences were well within the quoted errors. To avoid double counting of statistical and systematic errors, these were used as cross checks only.
- **Uncertainty on the estimation of the muon chamber efficiency.** Corrections to the MC muon chamber reconstruction efficiency were obtained from independent data samples and varied within their uncertainties ($\pm 5\%$).
- **Fake muon background.** The background from fake muons has been extensively studied [59] and is further constrained by the like-sign distribution of Fig. 4b, which is dominated by this background. Accordingly, it was varied by a factor 1.5 (–4%).
- **Luminosity measurement.** The uncertainty associated with the luminosity measurement for the 1996–2000 data taking periods used for this analysis was included ($\pm 2\%$).
- **Tracking.** All tracking-based cuts (p_{T} and mass cuts) were varied by their respective uncertainties. To avoid double counting of statistical uncertainties, the D^* -related systematics were taken from previous ZEUS DIS [82] and γp [83] analyses employing similar cuts, but with larger event samples. The cut on p_{T}^{μ} was varied by $\pm 40 \text{ MeV}$. This yielded a combined error of +6% and –4%.
- **Trigger acceptance.** The error on the trigger acceptance was evaluated by comparing the efficiencies of the different trigger chains in the data with each other and with the MC ($\pm 3\%$).
- **B^0 – \bar{B}^0 mixing.** The possible systematic effect due to the variation of the mixing rate was found to be negligible.

The total systematic uncertainty was obtained by adding the above contributions in quadrature.

8 Results

To present results from the combined data sets, the measurements from the 1996–1997 run at $\sqrt{s} = 300$ GeV have been corrected using the predicted cross-section ratio [1] of 1.06, to correspond to the higher centre-of-mass energy of 318 GeV. All cross sections are therefore quoted for $\sqrt{s} = 318$ GeV.

8.1 Visible cross sections

The first step is the extraction of visible cross sections for the $D^* \mu$ final state from beauty. The acceptance for the $D^* \rightarrow D^0 \pi_s \rightarrow (K\pi)\pi_s$ decay chain was unfolded using a branching fraction of $2.57 \pm 0.06\%$ [78]. The effective b branching fractions used in the different MC generators were corrected to those listed in Table 2 in order to account for their influence on the overall acceptance, and on the shape of the predicted beauty contributions.

The measured beauty fraction in the inclusive sample, corrected for detector acceptance and branching fractions, was used to obtain the cross section for the process $ep \rightarrow ebb\bar{X} \rightarrow eD^{*\pm} \mu X$ in the visible kinematic range $p_T^{D^*} > 1.9$ GeV, $-1.5 < \eta^{D^*} < 1.5$, $p_T^\mu > 1.4$ GeV and $-1.75 < \eta^\mu < 1.3$ as follows:

$$\begin{aligned} \sigma_{\text{vis}}(ep \rightarrow ebb\bar{X} \rightarrow eD^{*\pm} \mu X) \\ = 160 \pm 37(\text{stat.})_{-57}^{+30}(\text{syst.}) \text{ pb.} \end{aligned} \quad (5)$$

This includes both unlike- and like-sign $D^* \mu$ combinations. The leading-order cross sections predicted by PYTHIA and HERWIG in the same kinematic range are $\sigma_{\text{vis}}(ep \rightarrow ebb\bar{X} \rightarrow eD^* \mu X) = 80$ and 38 pb, respectively. The measured cross section is larger than, but compatible with, the FMNR \otimes PYTHIA NLO prediction

$$\begin{aligned} \sigma_{\text{vis}}^{\text{NLO}}(ep \rightarrow ebb\bar{X} \rightarrow eD^{*\pm} \mu X) \\ = 67_{-11}^{+20}(\text{NLO})_{-9}^{+13}(\text{frag.} \oplus \text{br.}) \text{ pb,} \end{aligned} \quad (6)$$

where the first error refers to the uncertainties of the FMNR parton-level calculation, and the second error refers to the uncertainties related to fragmentation and decay.

For the photoproduction subsample, a visible cross section in the kinematic range $Q^2 < 1$ GeV² and $0.05 < y < 0.85$ was obtained:

$$\begin{aligned} \sigma_{\text{vis},\gamma p}(ep \rightarrow ebb\bar{X} \rightarrow eD^{*\pm} \mu X) \\ = 115 \pm 29(\text{stat.})_{-27}^{+21}(\text{syst.}) \text{ pb.} \end{aligned} \quad (7)$$

This can be compared to the NLO prediction from FMNR \otimes PYTHIA,

$$\begin{aligned} \sigma_{\text{vis},\gamma p}^{\text{NLO}}(ep \rightarrow ebb\bar{X} \rightarrow eD^{*\pm} \mu X) \\ = 54_{-10}^{+15}(\text{NLO})_{-7}^{+10}(\text{frag.} \oplus \text{br.}) \text{ pb.} \end{aligned} \quad (8)$$

As in the inclusive case, the NLO prediction underestimates the measured cross section by about a factor of 2, but is compatible with the measurement (Table 3).

From the DIS sample, a visible cross section in the kinematic range $Q^2 > 2$ GeV², $0.05 < y < 0.7$ and $p_T^{D^*} > 1.5$ GeV (other D^* and muon cuts as for (5)) of

$$\begin{aligned} \sigma_{\text{vis,DIS}}(ep \rightarrow ebb\bar{X} \rightarrow eD^* \mu X) \\ = 58 \pm 29(\text{stat.})_{-20}^{+11}(\text{syst.}) \text{ pb} \end{aligned} \quad (9)$$

was obtained.

Again, the cross sections obtained from RAPGAP (used to compute acceptance corrections for the central signal extraction) and HERWIG (used for systematic checks, particularly with regard to differences in the $b\bar{b}$ correlations) in the same kinematic regime are considerably lower, $\sigma(ep \rightarrow ebb\bar{X} \rightarrow eD^* \mu X) = 26$ and 10 pb, respectively. An NLO prediction is not available for this kinematic region.

Table 3. Comparison of measured and predicted cross sections. For the measured cross sections, the first error is statistical, and the second is systematic. For the QCD prediction, the error is due to the parton-level NLO calculation convoluted with the uncertainties of fragmentation and decay to the visible final state. The number in parentheses refers to the corresponding equation for each cross section; see text. For the definition of the kinematic range of each cross section, see text

cross section	measured	NLO QCD	ratio
inclusive, visible, (5)	$160 \pm 37_{-57}^{+30}$ pb	67_{-14}^{+24} pb	$2.4_{-1.3}^{+0.9}$
γp , visible, (7)	$115 \pm 29_{-27}^{+21}$ pb	54_{-12}^{+18} pb	$2.1_{-1.0}^{+0.8}$
DIS, visible, (9)	$58 \pm 29_{-20}^{+11}$ pb	-	-
γp , vis. same b , (13)	$52 \pm 13_{-11}^{+9}$ pb	29_{-6}^{+9} pb	$1.8_{-0.8}^{+0.7}$
DIS, vis. same b , (15)	$28 \pm 14_{-10}^{+5}$ pb	-	-
γp , b quark, (16)	$11.9 \pm 2.9_{-3.3}^{+1.8}$ nb	$5.8_{-1.3}^{+2.1}$ nb	$2.0_{-1.1}^{+0.8}$
DIS, b quark, (17)	$3.6 \pm 1.8_{-1.4}^{+0.5}$ nb	$0.87_{-0.16}^{+0.28}$ nb	$4.2_{-2.9}^{+2.3}$
γp , b differential, (20)	$0.30 \pm 0.07_{-0.06}^{+0.05}$ nb/GeV	$0.16_{-0.02}^{+0.04}$ nb/GeV	$1.8_{-0.8}^{+0.7}$

8.2 Comparison to H1 results

A photoproduction cross section similar to (7) in a slightly different kinematic range, $p_T^{D^*} > 1.5$ GeV, $|\eta^{D^*}| < 1.5$, $p^\mu > 2.0$ GeV, $|\eta^\mu| < 1.735$, $Q^2 < 1$ GeV² and $0.05 < y < 0.75$ has been obtained by the H1 collaboration [39]

$$\begin{aligned} \sigma_{\text{vis},\gamma p}^{\text{H1}}(ep \rightarrow e b \bar{b} X \rightarrow e D^{*\pm} \mu X; \text{H1}) \\ = 206 \pm 53(\text{stat.}) \pm 35(\text{syst.}) \text{ pb.} \end{aligned} \quad (10)$$

The ZEUS cross section of (7) extrapolated to the same kinematic range as the H1 measurement using FMNR \otimes PYTHIA is

$$\begin{aligned} \sigma_{\text{vis},\gamma p}(ep \rightarrow e b \bar{b} X \rightarrow e D^{*\pm} \mu X; \text{H1}) \\ = 135 \pm 33(\text{stat.})_{-31}^{+24}(\text{syst.}) \text{ pb,} \end{aligned} \quad (11)$$

which is somewhat smaller, but in agreement within errors.

The corresponding FMNR \otimes PYTHIA NLO prediction is

$$\begin{aligned} \sigma_{\text{vis},\gamma p}^{\text{NLO}}(ep \rightarrow e b \bar{b} X \rightarrow e D^{*\pm} \mu X; \text{H1}) \\ = 61_{-12}^{+17}(\text{NLO})_{-8}^{+12}(\text{frag.} \oplus \text{br.}) \text{ pb.} \end{aligned} \quad (12)$$

This is larger than the NLO cross section evaluated by H1 [39] due to the inclusion of the hadron-like photon contribution, the inclusion of secondary-muon branching fractions for D^* and μ from the same b quark (Table 2), and a detailed simulation of the kinematics of the $b \rightarrow B \rightarrow D^*$ chain rather than direct collinear fragmentation of b quarks into D^* mesons. The data to NLO ratio is consistent with the results in the ZEUS kinematic range.

8.3 Cross sections for $D^* \mu$ from the same b quark

In all the cross sections evaluated above, a significant part of the systematic error arises from the fraction of the beauty contribution in the charm-enriched or like-sign regions, where it cannot be well measured ($\Delta R > 2$ region in Fig. 4a, b and d). This fraction depends on details of the description of $b\bar{b}$ correlations in the MC used for the signal extraction. In the beauty-enriched low- ΔR unlike-sign region, which dominates the fit of the beauty fraction, about 95% of the $D^* \mu$ pairs are produced from the same parent b quark. The systematic error can thus be reduced by reinterpreting the measurements in terms of cross sections for this subprocess only. The corresponding cross section for photoproduction of a D^* and μ from the same b quark (always unlike sign, same kinematic cuts as for (7)) is

$$\begin{aligned} \sigma_{\text{vis},\gamma p}(ep \rightarrow e b(\bar{b}) X, b(\bar{b}) \rightarrow e D^* \mu X) \\ = 52 \pm 13(\text{stat.})_{-11}^{+9}(\text{syst.}) \text{ pb} \end{aligned} \quad (13)$$

where $b(\bar{b})$ stands for the sum of b and \bar{b} cross sections, and all other cuts remain the same.

This can be compared with the NLO prediction

$$\begin{aligned} \sigma_{\text{vis},\gamma p}^{\text{NLO}}(ep \rightarrow e b(\bar{b}) X, b(\bar{b}) \rightarrow e D^* \mu X) \\ = 29_{-5}^{+8}(\text{NLO})_{-4}^{+5}(\text{frag.} \oplus \text{br.}) \text{ pb.} \end{aligned} \quad (14)$$

For the DIS kinematic range (same as (9))

$$\begin{aligned} \sigma_{\text{vis,DIS}}(ep \rightarrow e b(\bar{b}) X, b(\bar{b}) \rightarrow e D^* \mu X) \\ = 28 \pm 14(\text{stat.})_{-10}^{+5}(\text{syst.}) \text{ pb} \end{aligned} \quad (15)$$

is obtained.

8.4 Parton-level cross sections

For a direct comparison with the NLO parton-level predictions, the measured visible cross sections were extrapolated to b -quark level. In order to minimise the systematic error, the b -level cross section is quoted for individual b (or \bar{b}) production rather than for correlated $b\bar{b}$ -pair production, i.e. using the cross sections displayed in (13) and (15).

A significant fraction of the parent b quarks of the selected events is expected to have very low p_T^b values [59]. Therefore, cross sections with no cut on p_T^b have been measured. Furthermore, there is a strong correlation between the pseudorapidity of the $D^* \mu$ system and the rapidity of the parent b quark, $\zeta^b = \frac{1}{2} \ln \frac{E_b + p_{z,b}}{E_b - p_{z,b}}$. In order to reflect the limited angular acceptance of the detector for both the D^* and the muon, the cross-section measurement was restricted to $\zeta^b < 1$. In this range, restricted to photoproduction, the p_T^b and ζ^b distributions of PYTHIA (after parton showering) agree with the central NLO b -quark spectra from FMNR to within $\pm 15\%$ [59]. Therefore, PYTHIA was used to extrapolate the visible cross section for the photoproduction region. Similarly, the corresponding RAPGAP spectra for the DIS case agree [59] with the central NLO predictions from HVQDIS.

The acceptance for b quarks due to the kinematic cuts on the fragmentation and decay products ranges from $\sim 4\%$ at $p_T^b = 0$ GeV to $\sim 55\%$ at $p_T^b = 10$ GeV. The remaining part of the extrapolation is due to the relevant branching ratios.

The extrapolation implies additional systematic uncertainties from the b -quark fragmentation ($+5\% / -15\%$) and decay ($\pm 9\%$) and the details of the shape of the p_T^b spectrum ($\pm 5\%$). The extrapolation was calculated assuming the validity of the NLO p_T^b shape and is therefore valid only in the context of this theoretical framework; the uncertainty for the visible cross section corresponding to a potential deviation from this shape, namely the reweighting of the $p_T^{D^* \mu}$ spectrum, is removed. The result for the extrapolated cross section for $\zeta^b < 1$, $Q^2 < 1$ GeV², $0.05 < y < 0.85$ and $m_b = 4.75$ GeV was

$$\sigma_{\gamma p}(ep \rightarrow b(\bar{b}) X) = 11.9 \pm 2.9(\text{stat.})_{-3.3}^{+1.8}(\text{syst.}) \text{ nb.} \quad (16)$$

The corresponding result for the extrapolated cross section for $\zeta^b < 1$, $Q^2 > 2$ GeV², $0.05 < y < 0.7$ and $m_b = 4.75$ GeV was

$$\sigma_{\text{DIS}}(ep \rightarrow b(\bar{b}) X) = 3.6 \pm 1.8(\text{stat.})_{-1.4}^{+0.5}(\text{syst.}) \text{ nb.} \quad (17)$$

These cross sections are to be compared to the NLO prediction for the same kinematic range using the FMNR calculation of

$$\sigma_{\gamma p}^{\text{NLO}}(ep \rightarrow b(\bar{b}) X) = 5.8_{-1.3}^{+2.1} \text{ nb,} \quad (18)$$

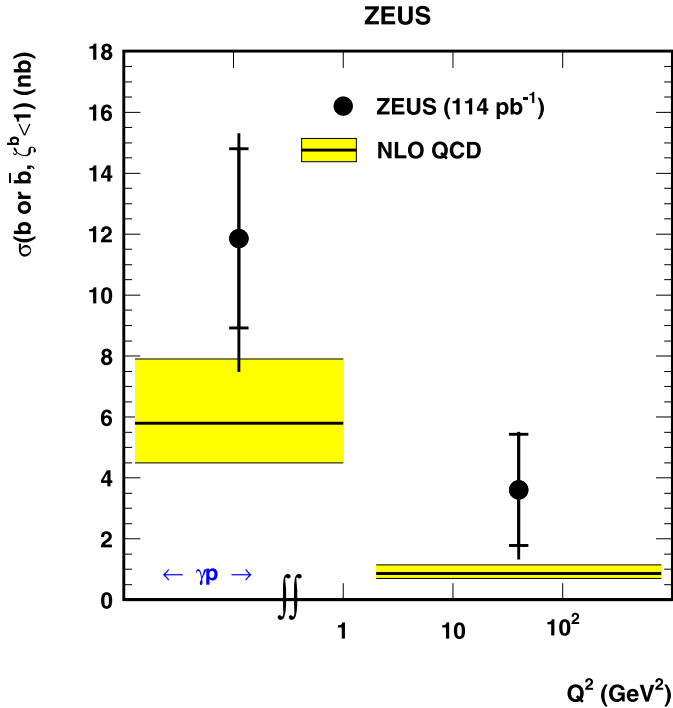


Fig. 6. Cross section for single b or \bar{b} -quark production in the rapidity range $\zeta^b < 1$ for photoproduction (*left*) and DIS (*right*), compared to NLO QCD predictions from FMNR (*left*) and HVQDIS (*right*). The γp cross section is for $0.05 < y < 0.85$, $Q^2 < 1 \text{ GeV}^2$ and the DIS cross section for $0.05 < y < 0.7$, $Q^2 > 2 \text{ GeV}^2$. The cross sections are integrated over the Q^2 ranges, and over the full p_T^b range

and to the NLO HVQDIS prediction of

$$\sigma_{\text{DIS}}^{\text{NLO}}(ep \rightarrow b(\bar{b})X) = 0.87^{+0.28}_{-0.16} \text{ nb}. \quad (19)$$

These cross sections are presented in Fig. 6. The ratio of measured to predicted cross sections in the photoproduction region remains the same as the ones obtained from the comparison at visible level (Table 3). This confirms the self-consistency of the extrapolation procedure used.

8.5 Comparison to previous ZEUS measurements

In order to compare the photoproduction cross section to previous ZEUS results [29, 30, 35–37], the cross sections (13) or equivalently (16), already referring to the production of a single b quark, need to be translated into a differential cross section, $\frac{d\sigma}{dp_T^b}$, in the pseudorapidity range $|\eta^b| < 2$ [35–37]. The median p_T^b value for events satisfying the cuts for (13) is 6.5 GeV [59]. The measured cross section, (13), is therefore extrapolated to this value using FMNR \otimes PYTHIA, yielding

$$\begin{aligned} \frac{d\sigma}{dp_T^b}(p_T^b = 6.5 \text{ GeV}, |\eta^b| < 2) \\ = 0.30 \pm 0.07(\text{stat.})^{+0.05}_{-0.06}(\text{syst.}) \text{ nb}. \end{aligned} \quad (20)$$

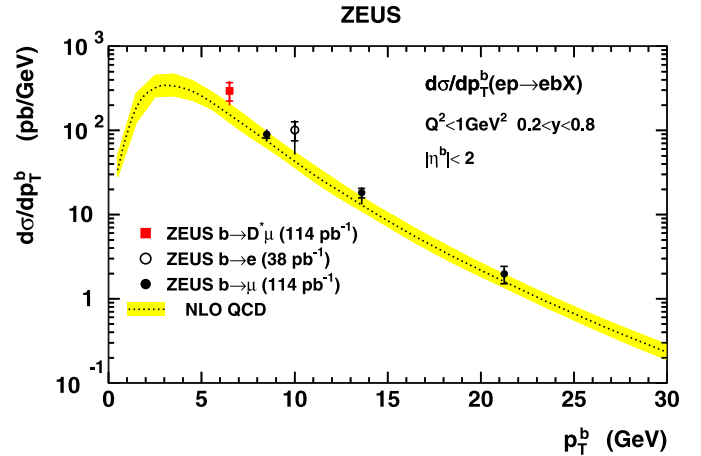


Fig. 7. Differential cross-section $\frac{d\sigma}{dp_T^b}$ of this analysis (*filled square*) compared to measurements from previous ZEUS analyses, after rescaling to the kinematic range indicated in the figure

This result is compared to theory and previous measurements in Fig. 7. It is higher than, but consistent with, these measurements.

9 Conclusions

Cross sections for beauty production in ep collisions at HERA have been measured in both the photoproduction and DIS regimes using an analysis technique based on the detection of a muon and D^* . Agreement is obtained with the corresponding H1 result. Since the analysis is sensitive to b -quark production near the kinematic threshold, the measured visible cross sections were extrapolated to b -quark cross sections without an explicit cut on p_T^b . Both at visible and at quark level, the measured cross sections exceed the NLO QCD predictions, but they are compatible within the errors. The data to NLO ratio is also larger than, but compatible with, previous ZEUS measurements of the b production cross section at higher p_T^b .

Acknowledgements. We thank the DESY Directorate for their strong support and encouragement. The remarkable achievements of the HERA machine group were essential for the successful completion of this work and are greatly appreciated. We are grateful for the support of the DESY computing and network services. The design, construction and installation of the ZEUS detector have been made possible owing to the ingenuity and effort of many people who are not listed as authors. It is also a pleasure to thank S. Frixione for help with the theoretical predictions.

References

1. S. Frixione et al., Nucl. Phys. B **412**, 225 (1994)
2. S. Frixione, P. Nason, G. Ridolfi, Nucl. Phys. B **454**, 3 (1995)

3. M. Cacciari, S. Frixione, P. Nason, JHEP **0103**, 006 (2001)
4. B.W. Harris, J. Smith, Nucl. Phys. B **452**, 109 (1995)
5. B.W. Harris, J. Smith, Phys. Lett. B **353**, 535 (1995)
6. B.W. Harris, J. Smith, Phys. Lett. B **359**, 423 (1995) [Erratum]
7. B.W. Harris, J. Smith, Phys. Rev. D **57**, 2806 (1998)
8. UA1 Collaboration, C. Albajar et al., Phys. Lett. B **186**, 237 (1987)
9. UA1 Collaboration, C. Albajar et al., Phys. Lett. B **256**, 121 (1991)
10. UA1 Collaboration, C. Albajar et al., Phys. Lett. B **262**, 497 (1991) [Erratum]
11. UA1 Collaboration, C. Albajar et al., Z. Phys. C **61**, 41 (1994)
12. CDF Collaboration, F. Abe et al., Phys. Rev. Lett. **71**, 500 (1993)
13. CDF Collaboration, F. Abe et al., Phys. Rev. Lett. **71**, 2396 (1993)
14. CDF Collaboration, F. Abe et al., Phys. Rev. Lett. **75**, 1451 (1995)
15. CDF Collaboration, F. Abe et al., Phys. Rev. D **53**, 1051 (1996)
16. CDF Collaboration, D. Acosta et al., Phys. Rev. D **65**, 052005 (2002)
17. CDF Collaboration, D. Acosta et al., Phys. Rev. D **71**, 032001 (2005)
18. D0 Collaboration, S. Abachi et al., Phys. Rev. Lett. **74**, 3548 (1995)
19. D0 Collaboration, B. Abbott et al., Phys. Lett. B **487**, 264 (2000)
20. D0 Collaboration, B. Abbott et al., Phys. Rev. Lett. **84**, 5478 (2000)
21. D0 Collaboration, B. Abbott et al., Phys. Lett. **85**, 5068 (2000)
22. L3 Collaboration, M. Acciarri et al., Phys. Lett. B **503**, 10 (2000)
23. L3 Collaboration, P. Achard et al., Phys. Lett. B **619**, 71 (2005)
24. WA78 Collaboration, M. Catanesi et al., Phys. Lett. B **202**, 453 (1988)
25. E672/E706 Collaboration, R. Jesik et al., Phys. Rev. Lett. **74**, 495 (1995)
26. E771 Collaboration, T. Alexopoulos et al., Phys. Rev. Lett. **82**, 41 (1999)
27. D.M. Jansen et al., Phys. Rev. Lett. **74**, 3118 (1995)
28. HERA-B Collaboration, I. Abt et al., Eur. Phys. J. C **26**, 345 (2003)
29. H1 Collaboration, C. Adloff et al., Phys. Lett. B **467**, 156 (1999)
30. ZEUS Collaboration, J. Breitweg et al., Eur. Phys. J. C **18**, 625 (2001)
31. H1 Collaboration, A. Aktas et al., Eur. Phys. J. C **40**, 349 (2005)
32. H1 Collaboration, A. Aktas et al., Eur. Phys. J. C **41**, 453 (2005)
33. H1 Collaboration, A. Aktas et al., Eur. Phys. J. C **45**, 23 (2006)
34. H1 Collaboration, A. Aktas et al., Eur. Phys. J. C **47**, 597 (2006)
35. ZEUS Collaboration, S. Chekanov et al., Phys. Rev. D **70**, 12008 (2004)
36. ZEUS Collaboration, S. Chekanov et al., Phys. Rev. D **70**, 012008 (2004)[hep-ex/0312057]
37. ZEUS Collaboration, S. Chekanov et al., Phys. Rev. D **74**, 059906 (2006) [Erratum]
38. ZEUS Collaboration, S. Chekanov et al., Phys. Lett. B **599**, 173 (2004)
39. H1 Collaboration, A. Aktas et al., Phys. Lett. B **621**, 56 (2005)
40. ZEUS Collaboration, U. Holm (ed.), The ZEUS Detector. Status Report (unpublished), DESY (1993), available on <http://www-zeus.desy.de/bluebook/bluebook.html>
41. N. Harnew et al., Nucl. Instrum. Methods A **279**, 290 (1989)
42. B. Foster et al., Nucl. Phys. B Proc. Suppl. **32**, 181 (1993)
43. B. Foster et al., Nucl. Instrum. Methods A **338**, 254 (1994)
44. M. Derrick et al., Nucl. Instrum. Methods A **309**, 77 (1991)
45. A. Andresen et al., Nucl. Instrum. Methods A **309**, 101 (1991)
46. A. Caldwell et al., Nucl. Instrum. Methods A **321**, 356 (1992)
47. A. Bernstein et al., Nucl. Instrum. Methods A **336**, 23 (1993)
48. A. Bamberger et al., Nucl. Instrum. Methods A **401**, 63 (1997)
49. ZEUS Collaboration, S. Chekanov et al., Eur. Phys. J. C **21**, 443 (2001)
50. G. Abbiendi et al., Nucl. Instrum. Methods A **333**, 342 (1993)
51. J. Andrusków et al., Preprint DESY-92-066, DESY (1992)
52. ZEUS Collaboration, M. Derrick et al., Z. Phys. C **63**, 391 (1994)
53. J. Andrusków et al., Acta Phys. Pol. B **32**, 2025 (2001)
54. ZEUS Collaboration, S. Chekanov et al., Nucl. Phys. B **729**, 492 (2005)
55. F. Jacquet, A. Blondel, in Proceedings of the Study for an ep Facility for Europe, ed. by U. Amaldi, p. 391, Hamburg, Germany (1979). Also in preprint DESY 79/48
56. T. Sjöstrand, Comput. Phys. Commun. **82**, 74 (1994)
57. H. Jung, Comput. Phys. Commun. **86**, 147 (1995)
58. G. Marchesini et al., Comput. Phys. Commun. **67**, 465 (1992)
59. A. Longhin, Ph.D. Thesis, Report DESY-THESIS-2004-050, Università di Padova and INFN, 2004
60. R. Brun et al., geant3, Technical Report CERN-DD/EE/84-1, CERN (1987)
61. J. Binnewies, B.A. Kniehl, G. Kramer, Z. Phys. C **76**, 677 (1997)
62. B.A. Kniehl, G. Kramer, M. Spira, Z. Phys. C **76**, 689 (1997)
63. J. Binnewies, B.A. Kniehl, G. Kramer, Phys. Rev. D **58**, 014014 (1998)
64. A. Lipatov, N. Zotov, Preprint hep-ph/0601240 (2006)
65. A. Lipatov, N. Zotov, Preprint hep-ph/0603017 (2006)
66. H. Jung, Phys. Rev. D **65**, 034015 (2002)
67. H. Jung, J. Phys. G **28**, 971 (2002)
68. CTEQ Collaboration, H.L. Lai et al., Eur. Phys. J. C **12**, 375 (2000)
69. M. Glück, E. Reya, A. Vogt, Phys. Rev. D **46**, 1973 (1992)
70. ZEUS Collaboration, A.E. Nuncio-Quiroz, Talk at XIV International Workshop on Deep Inelastic Scattering, Tsukuba, Japan, 20-24 April 2006 [to appear in the proceedings]
71. T. Sjöstrand, L. Lönnblad, S. Mrenna, Preprint hep-ph/0108264 (2001)

72. S. Frixione, B.R. Webber, JHEP **06**, 029 (2002)
73. S. Frixione, P. Nason, B.R. Webber, JHEP **08**, 007 (2003)
74. C. Peterson et al., Phys. Rev. D **27**, 105 (1983)
75. B. Andersson, G. Gustafson, B. Söderberg, Z. Phys. C **20**, 317 (1983)
76. B.R. Webber, Nucl. Phys. B **238**, 492 (1984)
77. T. Sjöstrand, Comput. Phys. Commun. **39**, 347 (1986)
78. Particle Data Group, S. Eidelman et al., Phys. Lett. B **592**, 1 (2004)
79. C.F. von Weizsäcker, Z. Phys. **88**, 612 (1934)
80. E.J. Williams, Phys. Rev. **45**, 729 (1934)
81. S. Frixione et al., Phys. Lett. B **319**, 339 (1993)
82. ZEUS Collaboration, S. Chekanov et al., Phys. Rev. D **69**, 012004 (2004)
83. ZEUS Collaboration, S. Chekanov et al., Phys. Lett. B **590**, 143 (2004)